Tight junctions in Schwann cells of peripheral myelinated axons: a lesson from claudin-19–deficient mice

Tatsuo Miyamoto,[1] Kazumasa Morita,[3] Daisuke Takemoto,[4] Kosei Takeuchi,[4,5] Yuka Kitano,[1] Tsuyoshi Miyakawa,[2] Kiyomi Nakayama,[6] Yasushi Okamura,[6] Hiroyuki Sasaki,[5,7] Yoshiki Miyachi,[3] Mikio Furuse,[1] and Shoichiro Tsukita[1]

[1]Department of Cell Biology, [2]Genetic Engineering and Functional Genomics Group, Horizontal Medical Research Organization, and [3]Department of Dermatology, Graduate School of Medicine, Kyoto University, Kyoto 606-8501, Japan
[4]Department of Biological Science, Graduate School of Science, Nagoya University, Nagoya 464-8602, Japan
[5]KAN Research Institute Inc., Kyoto Research Park, Chudoji, Shimogyo-ku, Kyoto 600-8317, Japan
[6]Section of Developmental Neurophysiology, Ozaki Institute for Integrative Bioscience, National Institute of Natural Sciences, Okazaki 444-8787, Japan
[7]Department of Molecular Cell Biology, Institute of DNA Medicine, The Jikei University School of Medicine, Nishi-Shinbashi, Minato-ku, Tokyo 105, Japan

Tight junction (TJ)–like structures have been reported in Schwann cells, but their molecular composition and physiological function remain elusive. We found that claudin-19, a novel member of the claudin family (TJ adhesion molecules in epithelia), constituted these structures. Claudin-19–deficient mice were generated, and they exhibited behavioral abnormalities that could be attributed to peripheral nervous system deficits. Electrophysiological analyses showed that the claudin-19 deficiency affected the nerve conduction of peripheral myelinated fibers. Interestingly, the overall morphology of Schwann cells lacking claudin-19 expression appeared to be normal not only in the internodal region but also at the node of Ranvier, except that TJs completely disappeared, at least from the outer/inner mesaxons. These findings have indicated that, similar to epithelial cells, Schwann cells also bear claudin-based TJs, and they have also suggested that these TJs are not involved in the polarized morphogenesis but are involved in the electrophysiological "sealing" function of Schwann cells.

Introduction

In vertebrates, a process called saltatory conduction causes action potentials to travel along myelinated axons faster than along nonmyelinated axons. Myelinated axons are tightly enwrapped by the continuous membrane layers of individual glial cells; i.e., Schwann cells in the peripheral nervous system (PNS) or oligodendrocytes in the central nervous system (CNS). Compaction of these layers leads to the formation of the myelin sheath, which electrically insulates axons. Along axons, these sheaths are interrupted at regularly spaced nodes of Ranvier, where axonal membranes can propagate action potentials. Saltatory conduction of action potentials occurs by jumping from node to node over individual myelin sheaths, and, for it to work efficiently, electrical insulation by Schwann cells/oligodendrocytes must be tightly established.

For this insulation, two distinct types of paracellular pathways must be electrically sealed: the axo-glial junctions at the paranode flanking the node of Ranvier and the intermembranous spaces within individual glial cells. Interestingly, the axo-glial paranodal junctions resemble septate junctions that are thought to be responsible for electrical sealing in invertebrates in general (Rosenbluth, 1976; Einheber et al., 1997); thus, this paranodal junction has attracted much interest in the past few years and the molecular architecture of this junction is being rapidly unraveled (Peles and Salzer, 2000; Pedraza et al., 2001; Spiegel and Peles, 2002; Poliak and Peles, 2003). On the other hand, the intermembranous spaces within individual glial cells have been considered to be mostly sealed by compact myelin, but, in addition, old electron microscopic observations indicated the existence of tight junction (TJ)–like structures that might also be involved in the intermembranous sealing of glial cells (Dermietzel, 1974; Mugnaini and Schnapp, 1974; Reale et al., 1975; Schnapp and Mugnaini, 1976; Sandri et al., 1977; Tabira et al., 1978; Dermietzel and Kroczek, 1980; Shinowara et al., 1980; see Fig. 2). However, a knowledge of the molecular components of these TJ-like structures in glial cells has been lacking for some time.

TJs have been identified and characterized in detail, mainly by using simple epithelial cells. TJs seal the paracellular routes of epithelial cells to create a primary barrier to the diffusion of solutes across the cellular sheet, and they also function as a boundary between the apical and basolateral membrane domains to produce their polarization (Anderson and Van Itallie, 1995; Balda and Matter, 1998; Tsukita et al., 2001; Anderson et al., 2004; Schneeberger and Lynch, 2004). On ultrathin section electron microscopy, TJs appear as a series of discrete sites of apparent fusion, involving the outer leaflets of the plasma membranes of adjacent cells (Farquhar and Palade, 1963). On freeze-fracture electron microscopy, TJs appear as a set of continuous, anastomosing intramembranous particle strands (TJ strands; Staehelin, 1974). These observations led to our current understanding of the three-dimensional structure of TJs; each TJ strand associates laterally with another TJ strand in apposing membranes of adjacent cells to form "paired" TJ strands where the intercellular space is completely obliterated (Tsukita et al., 2001).

To date, three distinct types of integral membrane proteins have been shown to localize at TJs: occludin (Furuse et al., 1993), junctional adhesion molecules (Martin-Padura et al., 1998), and claudins (Furuse et al., 1998a). Among them, claudin is now believed to be a major constituent of TJ strands (Tsukita and Furuse, 1999; Tsukita et al., 2001; Turksen and Troy, 2004). Claudins with molecular masses of ~23 kD bear four transmembrane domains and comprise a multigene family consisting of 24 members in mice/humans (Furuse et al., 1998a; Morita et al., 1999a,b,c; Simon et al., 1999; Tsukita and Furuse, 1999; Van Itallie and Anderson, 2004). Interestingly, when each claudin species was overexpressed in mouse L fibroblasts lacking endogenous claudins, exogenously expressed claudin molecules were polymerized within the plasma membrane to reconstitute paired TJ strands in cell–cell contact regions (Furuse et al., 1998b).

In myelinated axons of the CNS, TJ strand–like structures ~10 nm thick were observed between the lamellae of myelin sheaths by freeze-fracture electron microscopy (Dermietzel, 1974; Reale et al., 1975; Schnapp and Mugnaini, 1976; Tabira et al., 1978; Dermietzel and Kroczek, 1980). These interlamellar strands run parallel to the axon axis and run radially through the myelin sheath, consisting of the so-called 'radial component of myelin' (Peters, 1961, 1964; Dermietzel, 1974), and these radial components were speculated to be directly involved in electrically isolating the extracellular compartment within myelin sheaths (Mugnaini and Schnapp, 1974). When we discovered the existence of the claudin gene family, we noticed that claudin-11, which was initially identified as an oligodendrocyte-specific protein (OSP), constitutes these interlamellar strands (Morita et al., 1999b). Further, Gow et al. (1999) reported that mice lacking the expression of claudin-11/OSP lacked interlamellar strands in the myelinated axons of the CNS and exhibited characteristic neurological deficits.

Also in myelinated axons of the PNS, the existence of TJ strand–like structures has been reported in three regions of Schwann cells; strands existed between the apposed membranes of paranodal terminal loops and the Schmidt-Lanterman incisures, as well as those of outer/inner mesaxons (Sandri et al., 1977; Tetzlaff, 1978, 1982; Shinowara et al., 1980; Salzer, 2003; see Fig. 2 A). Interestingly, however, claudin-11 was not expressed in Schwann cells (Morita et al., 1999b), which leads to the intriguing question of whether these strands can also be regarded as TJ strands, and, if so, what species of claudins constitutes them. The identification of such claudin species has been regarded as important for a better understanding of the molecular basis to the physiology of Schwann cells.

In this study, we found that claudin-19 was expressed in large amounts in the PNS, not in the CNS, and constituted the TJ-like structures of Schwann cells that were detectable by electron microscopy. Furthermore, we generated claudin-19–deficient mice and found that they lacked TJs in Schwann cells. Through detailed analyses of these mice, we examined and discussed the functions of claudin-based TJs in Schwann cells.

Results

Claudin-19 as a constituent of TJs in the Schwann cells of peripheral myelinated nerves

Northern blotting revealed that claudin-19 was expressed in large amounts in the PNS. Other tissues, including the brain, did not give strong signals, but the kidney expressed this claudin in fairly large amounts (Fig. 1 A). Similar to other claudin species, claudin-19 showed an ability to polymerize to reconstituted TJ strand–like structures in cell–cell contact regions when overexpressed in mouse L fibroblasts (Fig. 1 B). These findings suggested that claudin-19 constituted TJ strands in some types of cells within peripheral nerves. In peripheral nerves, three types of cells have been reported to bear TJs or TJ-like structures: endothelial cells of blood vessels, mesothelial cells in the perineurium, and Schwann cells of myelinated axons.

To determine which types of cells in peripheral nerves expressed claudin-19, we first attempted to raise a specific pAb in rabbits using keyhole limpet hemocyanin–conjugated peptides that corresponded to the COOH-terminal tail of claudin-19 as an antigen. One of the affinity-purified pAbs appeared to be specific for claudin-19, as examined with Western blotting against GST fusion proteins with the cytoplasmic tails of claudin-1 to -16 (Fig. 1 C). This specificity was later confirmed in the analyses of claudin-19–deficient mice (see Fig. 6).

In contrast to claudin-19, claudin-11 was reported to be expressed in the CNS but not in the PNS (Morita et al., 1999b). We then examined the mutually exclusive expression patterns of claudin-11 and -19 in the nervous system by using immunofluorescence microscopy. Frozen sections of the mouse spinal cord with the ventral root were stained with anti–claudin-11 and anti–claudin-19 pAbs. As shown in Fig. 1 D, the signals for claudin-11 and -19 were completely restricted to the spinal cord (i.e., CNS) and the ventral root (i.e., PNS), respectively. Furthermore, close inspection revealed that claudin-19 was not detected in either the endothelial cells of blood vessels or in the mesothelial cells of the root perineurium, but its distribution appeared to be associated with relatively thick nerve fibers.
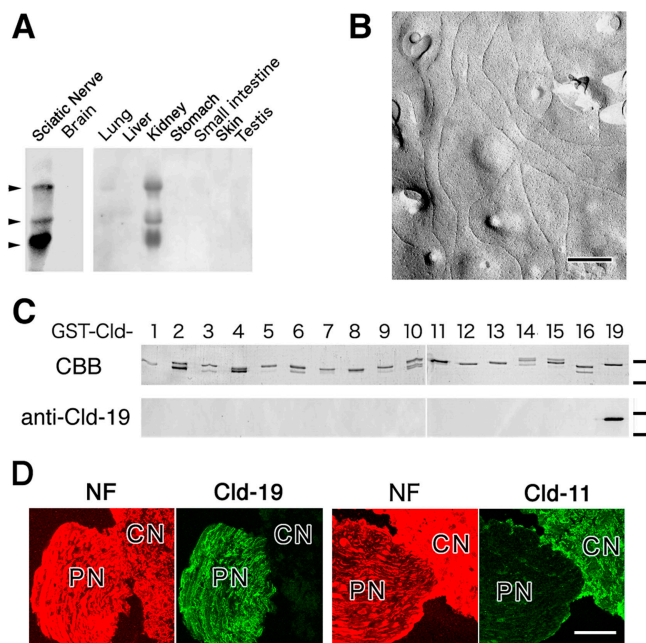
Figure 1. Abundant expression of claudin-19 in PNS. (A) Northern blots of mouse claudin-19 expression. Aliquots of total RNA (1 μg) isolated from the mouse sciatic nerve and the whole brain were separated and transferred onto a nylon membrane. This membrane (left) and mouse multiple tissue membranes (right; SeeGene) were probed with a digoxigenin-labeled claudin-19 RNA probe. Claudin-19 mRNAs were detected as major 1.0-kb and minor 4.7- and 1.8-kb bands (arrowheads) in large amounts in the sciatic nerve and the kidney. In the kidney, claudin-19 appeared to be expressed and concentrated at TJs in renal tubules, but, in this study, we did not discuss this point. (B) TJ strand–like structures reconstituted in L fibroblasts exogenously expressing mouse claudin-19. Freeze-fracture replica electron microscopy identified these strands in the cell–cell contact regions. Bar, 500 nm. (C) Specificity of anti–claudin-19 pAb. GST fusion proteins with the cytoplasmic domains of claudin-1 to -16 as well as the cytoplasmic domain of claudin-19 were produced in *E. coli*. The lysates of *E. coli* were separated by SDS-PAGE (CBB), followed by immuno-blotting with anti–claudin-19 pAb, which was raised in this study. Bars indicate molecular masses of 31 and 21 kD from the top. (D) PNS-specific expression of claudin-19. Transverse frozen sections of the mouse spinal cord with the ventral root were double stained with antineurofilament mAb (red)/anti–claudin-19 pAb (green) or antineurofilament mAb (red)/anti–claudin-11 pAb (green). In the nervous system, the expression of claudin-19 was restricted to the PNS (PN). In contrast, as previously reported (Morita et al., 1999b), claudin-11 was expressed in the CNS (CN) but not in the PNS (PN). Bar, 50 μm.

We then examined the distribution of claudin-19 in peripheral nerves in more detail. When single fibers teased from sciatic nerves were whole-mount stained with anti–claudin-19 pAb, all of the myelinated axons showed characteristic staining patterns (Fig. 2 B). As schematically drawn in the left panel of Fig. 2 A, TJ strand–like structures have been reported to form a circumferential belt and to occur along incisures on both sides of individual, unrolled flat Schwann cells (Arroyo and Scherer, 2000; Poliak et al., 2002; Spiegel and Peles, 2002; Salzer, 2003). When these cells are rolled around axons, the strand on one side of each Schwann cell has been thought to make a paired strand with that on its other side; i.e., to form TJ-like junctions, the localization of which is very peculiar and three-dimensionally complex in internodal segments (Fig. 2 A, right). Interestingly, the claudin-19 staining

pattern of myelinated axons appeared to coincide with this peculiar, complex localization of the TJ-like structures of Schwann cells (Fig. 2 B). In the paranodal region, strong claudin-19 signals were detected, which may correspond to TJ-like structures that were observed between the paranodal terminal loops of Schwann cells. Consistent with this notion, claudin-19 was found to be more outwardly distributed than contactin-associated protein (Caspr)/Paranodin when the paranodal region of single myelinated fibers was double stained for claudin-19 and Caspr/Paranodin (a specific marker for the axo-glial paranodal junctions; Fig. 2 B, bottom). Claudin-19 was also highly concentrated at Schmidt-Lanterman incisures, where TJ-like structures were again shown to occur by electron microscopy. Furthermore, in most of the individual rolled Schwann cells, two continuous claudin-19–positive lines ran parallel to the axon axis between two paranodal regions, sometimes in a spiral manner. These may correspond to TJ-like structures that were observed at the outer and inner mesaxons of Schwann cells. It is safe to say that claudin-19 constitutes the TJ strand–like structures observed in Schwann cells by freeze-fracture replica electron microscopy, and that these structures can be regarded as a variant of the TJ strands found in many other epithelial/endothelial cells.

Generation of claudin-19–deficient mice

To explore the function of claudin-19 in vivo, we produced mice unable to express it. Nucleotide sequencing, as well as restriction mapping, identified four exons that cover the whole ORF of claudin-19 (Fig. 3 A). We constructed a targeting vector, which was designed to disrupt the claudin-19 gene by replacing all of these exons (exons 1–4) with the neomycin resistance gene. Two distinct lines of mice were generated from distinct embryonic stem (ES) cell clones in which the claudin-19 gene was disrupted by homologous recombination. Southern blotting confirmed the disruption of the claudin-19 gene in heterozygous as well as in homozygous mutant mice (Fig. 3 B), and RT-PCR detected no claudin-19 mRNA from the kidney of homozygous mutant mice (Fig. 3 C). Because both lines of mice showed the same phenotypes, we will mainly present data obtained from one line.

No obvious phenotype was apparent in heterozygous mutant mice, and when these mice were interbred, wild-type ($Cld19^{+/+}$), heterozygous ($Cld19^{+/-}$), and homozygous ($Cld19^{-/-}$) mutant mice were produced in the expected Mendelian ratios. $Cld19^{-/-}$ mice were developed, grew normally in the laboratory environment, and showed no differences in weight, size, or reproductive ability from $Cld19^{+/+}$ mice up to 2 yr of age.

Functional analyses of claudin-19–deficient mice

$Cld19^{-/-}$ mice appeared to walk awkwardly on a smooth surface, especially on a smooth rod. Therefore, we subjected these mice (∼10–13–wk-old male $Cld19^{+/+}$ and $Cld19^{-/-}$ mice) to several established behavioral tests (Fig. 4). First, a "beam test" was performed, in which we counted how many times a hindlimb slips while a mouse is walking a given distance on a thin or thick bar. Interestingly, $Cld19^{-/-}$ mice exhibited

Figure 2. **Subcellular distribution of claudin-19 in peripheral myelinated axons.** (A) Schematic view of a myelinated axon in the PNS. In the left panel, one myelinating Schwann cell has been unrolled, revealing the regions that form compact myelin (asterisks), the outer mesaxon (OMA), the inner mesaxon (IMA), the Schmidt-Lanterman incisures (SL), and the paranode (PN). On both sides of individual, unrolled flat Schwann cells, TJ strand–like structures have been reported to form a circumferential belt and also to occur along incisures. Continuous and dotted green lines represent these strands on this and the far side of unrolled cells, respectively. When these cells are rolled around axons (right), the continuous line makes paired strands with the dotted line on the other side to form TJ-like structures, the localization of which in the internodal segment is very complex. TJ-like structures are densely and spirally concentrated at the Schmidt-Lanterman incisures (SL) and the paranode, and occur as two parallel lines along outer (1) and inner (2) mesaxons. (B) Whole-mount double staining of teased sciatic nerve fibers of 10-wk-old, wild-type mice with anti–claudin-19 pAb (green) and antineurofilament mAb (red). The distribution of claudin-19 coincided well with the expected localization of TJ-like structures presented in the right panel of A. Single arrowheads, paranodal regions; double arrowheads, Schmidt-Lanterman incisures; arrows, outer/inner mesaxons. In the bottom panel, one nodal/paranodal region was double stained with rat Caspr/Paranodin-pAb (red) and rabbit anti–claudin-19 pAb (green). Note that at the paranode, claudin-19 was more outwardly distributed than Caspr/Paranodin. Bars: (top) 5 μm; (bottom) 3 μm.
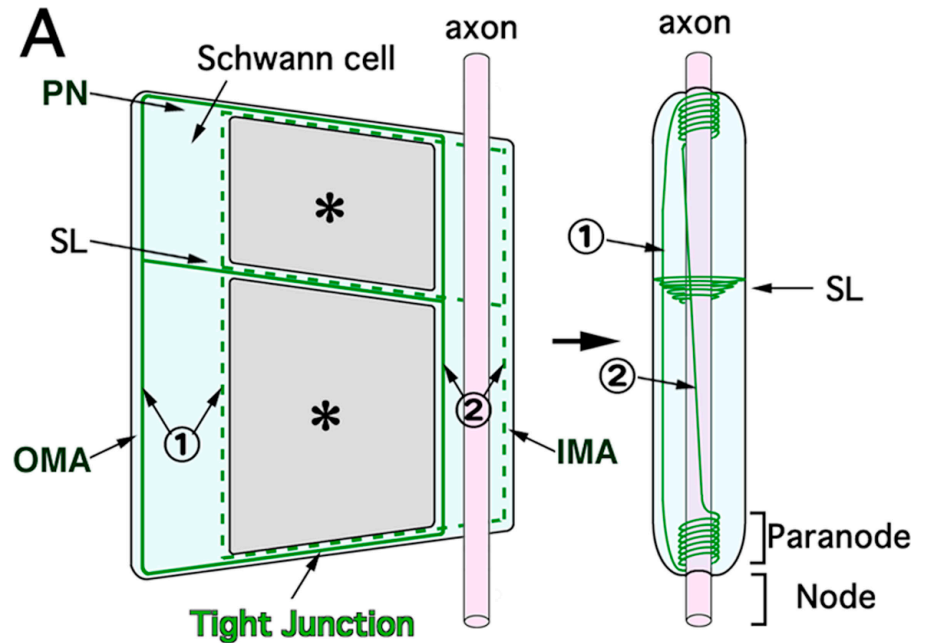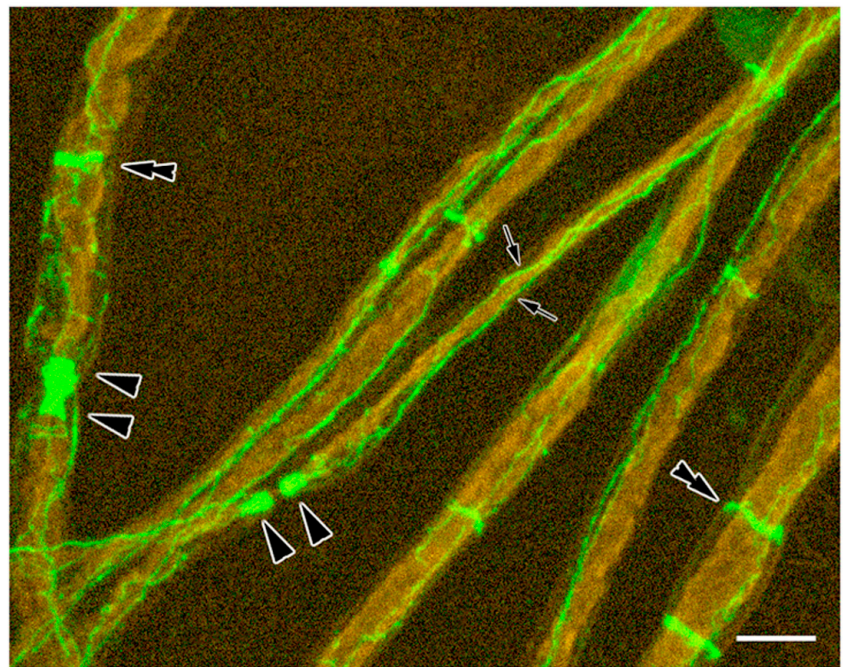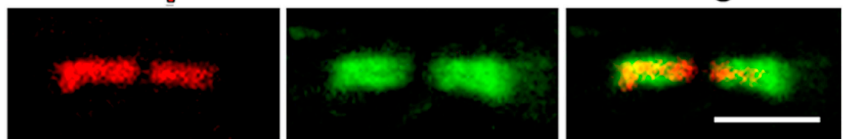

significantly more slips on these bars than $Cld19^{+/+}$ mice. Second, these mice were subjected to a "rotarod test." In this test, mice were put on a rotating rod, and how long they remained on the rod was measured. $Cld19^{-/-}$ mice fell from the rod more quickly than $Cld19^{+/+}$ mice. Importantly, in both tests, but especially in the rotarod test, $Cld19^{-/-}$ mice performed better as the trials were repeated (similar to $Cld19^{+/+}$ mice), which was consistent with the notion that the neuronal
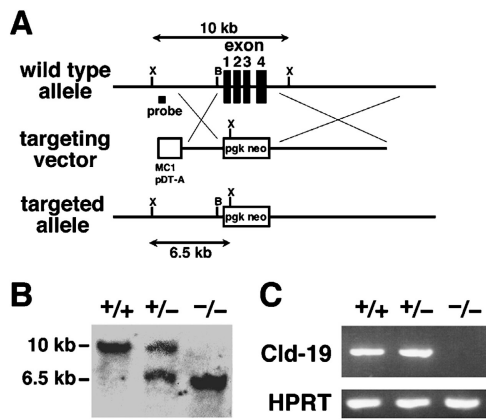
Figure 3. **Generation of claudin-19–deficient mice.** (A) Construction of the wild-type allele, the targeting vector, and the targeted allele of the mouse claudin-19 gene. Four exons covered the whole ORF of claudin-19, and the targeting vector contained the pgk-neo cassette in its middle portion to delete all of these exons in the targeted allele. The position of the probe for Southern blotting is indicated as a bar. MC1pDT-A, diphthelia toxin A expression cassette; X, XbaI; B, BamHI. (B) Genotype analyses by Southern blotting of XbaI-digested genomic DNA from wild-type (+/+), heterozygous (+/−), and homozygous (−/−) mice for the mutant claudin-19 gene allele. Southern blotting with the probe (A) yielded a 10-kb and a 6.5-kb band from the wild-type and targeted allele, respectively. (C) Loss of claudin-19 mRNA in the kidney of claudin-19–deficient mice examined by RT-PCR. As a control, the hypoxanthine phosphoribosyl transferase gene was equally amplified in all samples.

deficits of $Cld19^{-/-}$ mice observed in these tests were attributable to defects in the PNS. Furthermore, to evaluate CNS functions in $Cld19^{-/-}$ mice, we performed two more behavior tests, the "open field test" and the "prepulse inhibition test" (see Materials and methods). In these tests, no behavioral abnormalities were detected in $Cld19^{-/-}$ mice. Thus, taking the PNS-specific expression of claudin-19 in the nervous system into consideration, we concluded that $Cld19^{-/-}$ mice suffered from a kind of peripheral neuropathy.

To directly evaluate the electrophysiological properties of the peripheral nerves in $Cld19^{-/-}$ mice, we made field potential recordings of isolated sciatic nerves to measure the compound action potentials (CAPs), though this recording was not technically easy mainly because of the short length of isolated mouse sciatic nerves. When nerves were stimulated with sufficiently large currents to elicit the maximal CAP amplitude, CAPs obtained from $Cld19^{+/+}$ mice demonstrated a single-peak, smooth waveform. In 7 out of 10 $Cld19^{-/-}$ mice, CAP waveforms or population conduction velocities did not appear to be significantly different from those in $Cld19^{+/+}$ mice, but in three $Cld19^{-/-}$ mice we noticed a significant difference in CAP waveforms. These CAPs showed a characteristic double-peak waveform: a peak around a normal conduction velocity and an additional delayed peak (Fig. 5). Interestingly, under the stimulus intensity to elicit half-maximal CAP amplitude, this double-peak CAP waveform was reproducibly detected in $Cld19^{-/-}$ mice ($n = 10$) but never in $Cld19^{+/+}$ mice ($n = 10$; unpublished data). Although the mechanism responsible for this difference remains unclear, it is safe to say that the claudin-19 deficiency changed the conduction parameters of at least a subpopulation of myelinated fibers to reduce their conduction velocity.
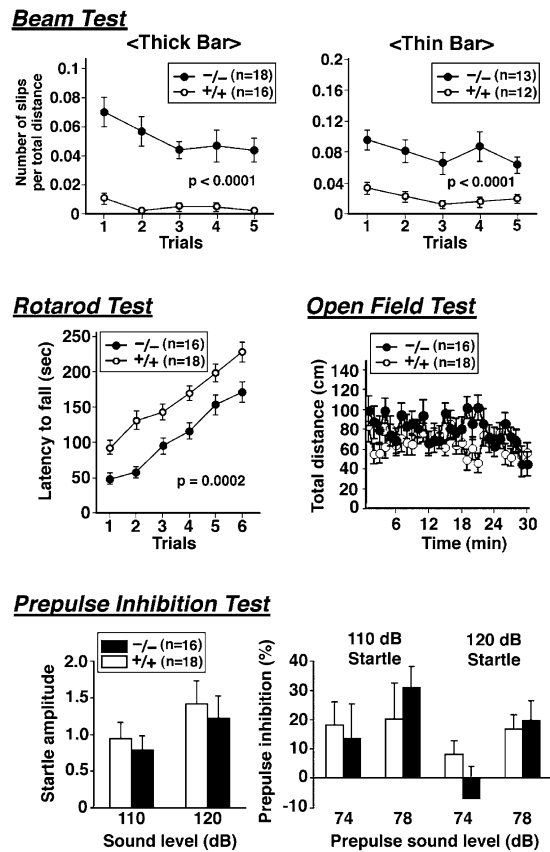

Figure 4. **Behavioral abnormalities in claudin-19–deficient mice.** All behavioral tests were performed with male $Cld19^{+/+}$ and $Cld19^{-/-}$ mice that were ~10–13–wk old at the start of the testing. Details of each test were described in Materials and methods. In the beam test, both on thick and thin bars, $Cld19^{-/-}$ mice exhibited significantly more frequent slips than $Cld19^{+/+}$ mice ($P < 0.0001$). In the rotarod test, $Cld19^{-/-}$ mice dropped from the rotating rod more quickly than $Cld19^{+/+}$ mice ($P = 0.0002$). In these tests, especially in the rotarod test, the performance of both $Cld19^{+/+}$ and $Cld19^{-/-}$ mice improved as the trials were repeated, suggesting that the neuronal deficits of $Cld19^{-/-}$ mice observed in these tests were not attributed to the defects in the CNS but to those in the PNS. Consistent with this, in the open field test, the total distance traveled during 30 min was not significantly different between $Cld19^{+/+}$ and $Cld19^{-/-}$ mice. Vertical activity and time spent in the center or the beam-break count for stereotyped behavior were not affected by the claudin-19 deficiency (not depicted). Finally, the prepulse inhibition test was performed to examine the extent to which the startle response of mice to the stimulus sound (110 or 120 dB) was inhibited by the prepulse stimulus sound (74 or 78 dB). The startle amplitude itself was not different between $Cld19^{+/+}$ and $Cld19^{-/-}$ mice, and the inhibition by prepulse stimuli was not significantly affected in $Cld19^{-/-}$ mice. The data obtained from the open field test and prepulse inhibition test again suggested that $Cld19^{-/-}$ mice suffered from a kind of peripheral neuropathy.

Morphological analyses of claudin-19–deficient mice

We then examined the morphology of PNS myelinated axons in $Cld19^{-/-}$ mice. First, in order to preserve the structure of axons as perfectly as possible, especially that of compact myelin, we fixed the saphenous nerves with chemical fixatives according to a method described previously (Tsukita and Ishikawa, 1980) and compared transverse sectional views of electron micrographs between $Cld19^{+/+}$ and $Cld19^{-/-}$ mice (Fig. 6 A, left). At a low magnification, no difference was discerned in terms of myelination. The ratios of axonal diameter to total fi-

Figure 5. **Electrophysiological analysis of claudin-19–deficient mice.** Sciatic nerves were isolated from 10-wk-old mice ($n = 10$ each for $Cld19^{+/+}$ and $Cld19^{-/-}$ mice), and field potential recordings were made to measure the CAPs. The distance between extracellular stimulation and recording electrodes was 2.5 cm. When nerves were stimulated with sufficiently large currents to elicit maximal CAP amplitude, CAPs obtained from all $Cld19^{+/+}$ mice demonstrated a single-peak, smooth waveform (open arrowheads; $+/+$). However, in 3 out of 10 $Cld19^{-/-}$ mice, CAPs showed a characteristic double-peak waveform: a peak around a normal conduction velocity (open arrowheads) and an additional delayed peak (closed arrowheads; $-/-$). Under the stimulus intensity to elicit half-maximal CAP amplitude, this double-peak CAP waveform was reproducibly detected in $Cld19^{-/-}$ mice, but never in $Cld19^{+/+}$ mice (not depicted). Arrows, stimulation.
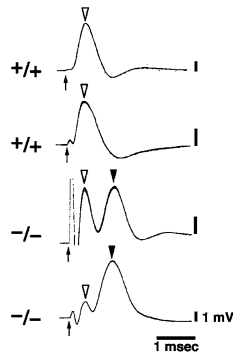
ber diameter (g values) of 35 myelinated axons randomly selected from two 15-wk-old $Cld19^{+/+}$ or $Cld19^{-/-}$ mice were found to be 0.60 ± 0.01 or 0.59 ± 0.01, respectively. Nevertheless, when transverse frozen sections of peripheral nerves (sciatic nerves) were immunofluorescently stained with anti–claudin-19 pAb, $Cld19^{+/+}$ myelinated axons were character-

ized by two clear, positive signals corresponding to the outer and inner mesaxons, whereas no signals were detected from $Cld19^{-/-}$ axons (Fig. 6 A, right). In each myelinated axon, E-cadherin was previously reported to be concentrated as numerous puncta along the outer surface of the Schwann cell and as a single dot at the inner mesaxon (Fannon et al., 1995). Then, we compared the distribution of claudin-19 with that of E-cadherin in transverse frozen sections of sciatic nerves (Fig. 6 B). In each $Cld19^{+/+}$ myelinated axon, claudin-19 was concentrated at one of the largest E-cadherin–positive puncta on the Schwann cell surface (outer mesaxon) as well as at the inner mesaxon. In $Cld19^{-/-}$ axons, claudin-19 seemed to disappear silently without affecting the distribution of E-cadherin; i.e., the organization of autotypic adherens junctions of Schwann cells. Furthermore, as far as was observed up to 2 yr after birth, no typical demyelination was detected in $Cld19^{-/-}$ PNS.

The claudin-19 deficiency did not appear to affect the overall organization of the node of Ranvier (Fig. 7). In longitudinal sections of myelinated nerves in both $Cld19^{+/+}$ and $Cld19^{-/-}$ axons, the nodal region was clearly discernible between the terminal loops of Schwann cells. Although whole-mount immunostaining revealed that in $Cld19^{-/-}$ myelinated axons, claudin-19

Figure 6. **Overall morphology of internodal segments of peripheral myelinated axons of claudin-19–deficient mice.** (A) Transverse sectional views of peripheral nerves of $Cld19^{+/+}$ and $Cld19^{-/-}$ mice. (left) The saphenous nerves were examined by ultrathin section electron microscopy. No significant difference was discerned in the myelination between $Cld19^{+/+}$ and $Cld19^{-/-}$ mice (see g values in the text). (right) Transverse frozen sections were cut from the sciatic nerves and were triple stained with anti–claudin-19 pAb (green), anti–myelin basic protein mAb (red), and antineurofilament pAb (blue). In the $Cld19^{+/+}$ sciatic nerve, two claudin-19–positive spots were detectable in each myelinated axon, which may correspond to the outer (arrows) and inner (arrowheads) mesaxons (see Fig. 8 a). In the $Cld19^{-/-}$ sciatic nerve, claudin-19 appeared to be simply removed without affecting the overall morphology of myelinated axons. (B) Claudin-19 and E-cadherin in myelinated axons. Transverse frozen sections were cut from $Cld19^{+/+}$ and $Cld19^{-/-}$ sciatic nerves and were triple stained with anti–E-cadherin mAb (red), anti–claudin-19 pAb (green), and antineurofilament pAb (blue). In each $Cld19^{+/+}$ myelinated axon, claudin-19 was concentrated at one of the largest E-cadherin–positive puncta on the Schwann cell surface; i.e., outer mesaxon (arrows) as well as at inner mesaxon (arrowheads). In $Cld19^{-/-}$ axons, claudin-19 disappeared without affecting the distribution of E-cadherin. Bars: (A, left) 2 μm; (A, right) 5 μm; (B) 5 μm.
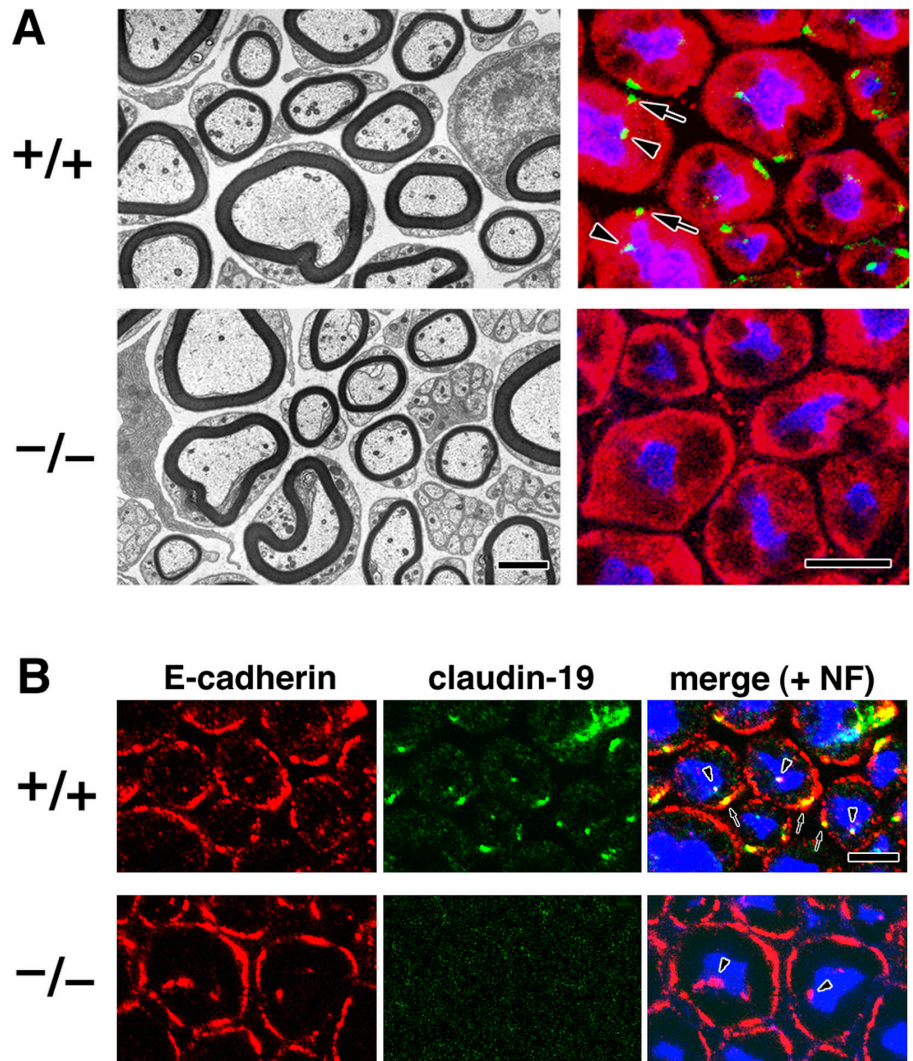
was completely undetectable in paranodal regions (unpublished data), the terminal loops appeared to be normal. Unfortunately, however, it was technically difficult to conclusively demonstrate the existence and/or absence of TJ-like structures between these loops of $Cld19^{+/+}$ and $Cld19^{-/-}$ axons by ultrathin section and by freeze-fracture replica electron microscopy. Importantly, also in the paranodal region of $Cld19^{-/-}$ axons, electron-dense transverse bands between terminal loops and axonal membranes were observed with a normal appearance.

Next, we closely compared the transverse sectional images of the internodal portion between $Cld19^{+/+}$ and $Cld19^{-/-}$ myelinated axons. The overall structure of the internodal portion of $Cld19^{-/-}$ myelinated axons appeared to be indistinguishable from that of $Cld19^{+/+}$ axons (Fig. 8 a). However, close inspection identified a clear difference in the outer and inner mesaxons between $Cld19^{+/+}$ and $Cld19^{-/-}$ axons. At the outer mesaxon of $Cld19^{+/+}$ axons, without exception, one to three "kissing points" of TJs, where the extracellular space was completely obliterated, were observed (Fig. 8 b). In contrast, the outer mesaxon of $Cld19^{-/-}$ axons lacked these kissing points completely, leaving widened intercellular gaps between apposed Schwann cell membranes (Fig. 8 b'). Consistent with this finding, TJ strand–like structures were frequently observed at the outer mesaxon of $Cld19^{+/+}$ axons, but were never observed in $Cld19^{-/-}$ axons (Fig. 8, c and c'). At the inner mesaxon of $Cld19^{+/+}$ axons, one kissing point of TJs was usually observed, though in some axons this kissing point was difficult to distinguish from the compact myelin (Fig. 8 d). At the inner mesaxon of $Cld19^{-/-}$ axons, typical kissing points were never detectable (Fig. 8 d'). Therefore, we concluded that in the $Cld19^{-/-}$ PNS, TJs themselves completely disappeared from myelinated Schwann cells (at least from their outer/inner mesaxons) without affecting their overall, peculiar cellular morphology.

Discussion

In multicellular organisms, the internal environment must be divided into various, compositionally distinct fluid compartments. This compartmentalization is usually established by cellular sheets of epithelia/endothelia that function as diffusion barriers to maintain the internal environment of each compartment. Multiple cells constitute these cellular sheets; thus, for these sheets to function as barriers, there must be some seal to the diffusion of solutes through the paracellular pathway. TJs have been shown to be responsible for this intercellular sealing in vertebrates (Anderson and Van Itallie, 1995; Balda and Matter, 1998; Tsukita et al., 2001; Anderson et al., 2004; Schneeberger and Lynch, 2004). The myelin sheath in the CNS/PNS constitutes a very peculiar compartment; each compartment is established by a single cell, an oligodendrocyte in the CNS, and a Schwann cell in the PNS together with the axon. To establish this unique compartment, the paracellular pathways within individual oligodendrocytes/Schwann cells are mostly sealed by compact myelin, whereas in the region of paranodal loops and Schmidt-Lanterman incisures, where compact myelin is absent, they must be sealed by other types of structures (Arroyo and Scherer, 2000; Poliak et al., 2002; Spiegel and Peles, 2002; Salzer, 2003). Indeed, to date, electron microscopy has revealed the occurrence of TJ-like structures at these loops and incisures in addition to the outer and inner mesaxons (Fig. 2 A). However, a lack of information on TJ-specific cell adhesion molecules in the epithelia/endothelia has long hampered clarification of whether these structures can really be regarded as a variant of TJs both structurally and functionally. Set against this background, the claudin family, which was initially thought to consist of 16 members (Morita et al., 1999a; Simon et al., 1999; Tsukita and Furuse, 1999), was identified in the epithelia as major constituents of TJ strands. Among the claudins, it was claudin-11, which had been identified as an OSP, that constituted the TJ-like structures of oligodendrocytes (Morita et al., 1999b), and analyses with knockout mice suggested that these TJs were functionally indispensable for CNS myelinated axons (Gow et al., 1999).

Interestingly, however, claudin-11 was not expressed in the PNS. Therefore, for a better understanding of the physiology of Schwann cells in the PNS, the question of whether the
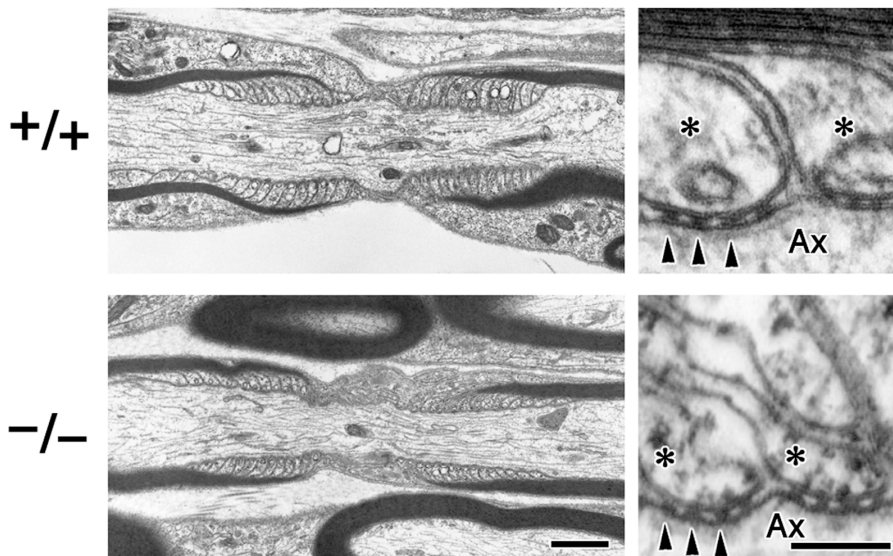

Figure 7. **Overall morphology of the node of Ranvier of peripheral myelinated axons of claudin-19–deficient mice.** Longitudinal sectional views of the node of Ranvier were compared by ultrathin section electron microscopy between $Cld19^{+/+}$ and $Cld19^{-/-}$ saphenous nerves. The claudin-19 deficiency did not appear to affect the overall morphology of the node of Ranvier, including the paranodal region (left). At a higher magnification in the paranodal region of both $Cld19^{+/+}$ and $Cld19^{-/-}$ axons, electron-dense transverse bands between terminal loops and axonal membranes were clearly observed (arrowheads). Asterisks, paranodal terminal loops; Ax, axon. Bars: (left) 1 μm; (right) 100 nm.

Figure 8. Absence of TJs in peripheral myelinated axons of claudin-19–deficient mice. Nerves were fixed with a fixative containing 0.1% tannic acid to clearly visualize the kissing points of TJs. (a) Transverse sectional electron microscopic view of *Cld19**+/+* myelinated axons. Outer and inner mesaxons (boxed areas) are shown in b and d, respectively. Ax, axon; My, myelin sheath. (b and b') Ultrathin section electron microscopy of outer mesaxons. In *Cld19+/+* myelinated axons, approximately one to three kissing points of TJs (arrowheads) were observed, whereas the outer mesaxons of *Cld19−/−* myelinated axons completely lacked these kissing points, leaving widened intercellular gaps between apposed Schwann cell membranes (arrow). Asterisks, outer mesaxons. (c and c') Freeze-fracture electron microscopy of outer mesaxons. Consistent with the images in b and b', TJ strand–like structures (arrowheads) were frequently observed at the outer mesaxon (asterisks) of *Cld19+/+* axons, but never at *Cld19−/−* axons (arrow). (d and d') Ultrathin section electron microscopy of inner mesaxons. The inner mesaxon of *Cld19+/+* myelinated axons (asterisk) usually bore one kissing point of TJs (arrowhead), whereas in the inner mesaxons of *Cld19−/−* myelinated axons, typical kissing points were never detectable (arrow). Bars: (a) 200 nm; (b and b') 100 nm; (c and c') 200 nm; (d and d') 100 nm.
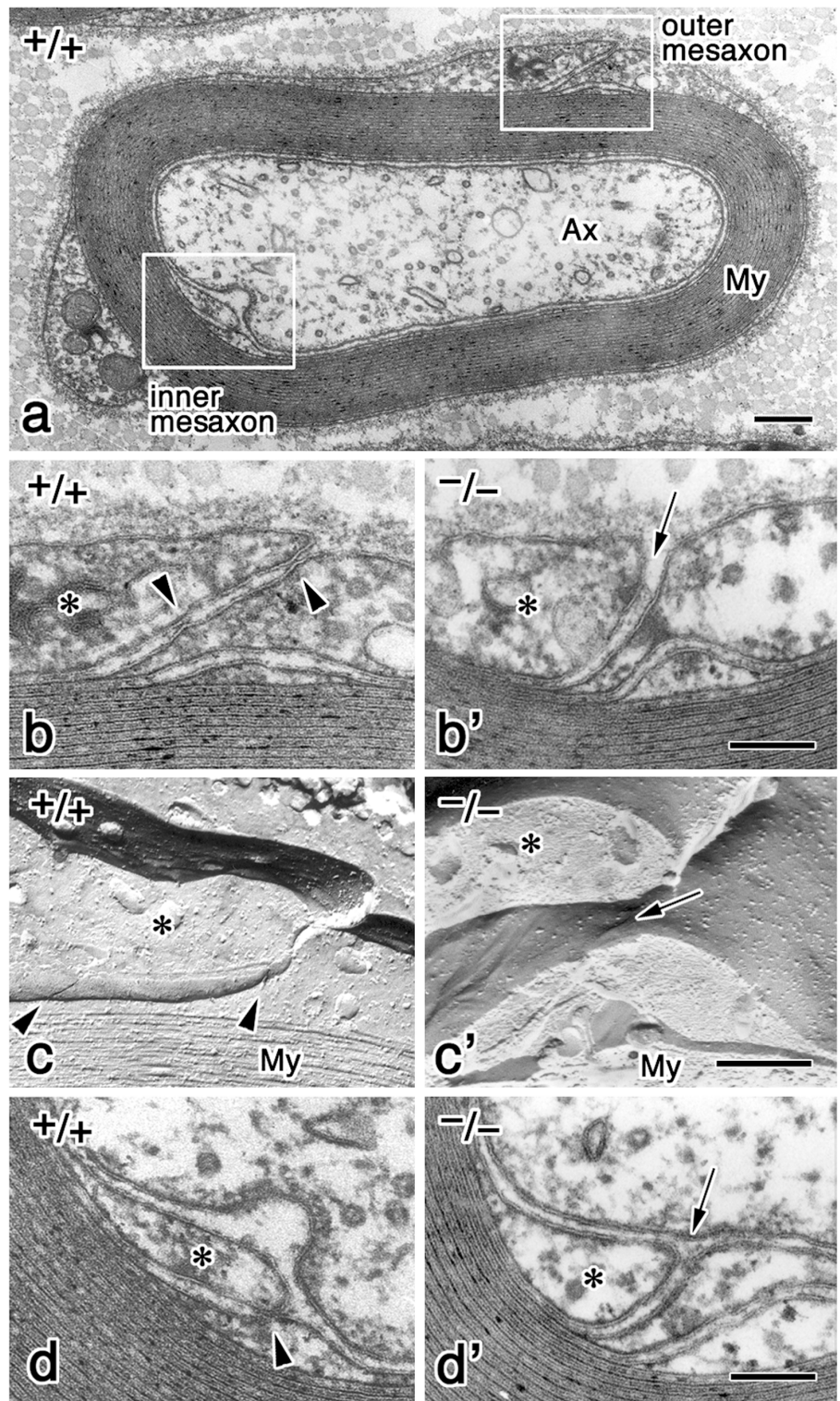
TJ-like structures reported in Schwann cells can be regarded as TJs both structurally and functionally, and if so, what species of claudins constitute them, needs to be answered. Along this line, claudins expressed in Schwann cells were searched for by RT-PCR using mouse sciatic nerve RNA with primers for claudin-1 to -16 (Poliak et al., 2002). As a result, claudin-1, -2, -5, -10, and -15 were identified, and immunofluorescence micros-copy showed that claudin-1 and -5 were concentrated at paranodal loops/mesaxons and Schmidt-Lanterman incisures, respectively. However, our anti–claudin-1 pAbs did not give any specific signals from the myelinated nerves of the PNS, and claudin-5 was detected very clearly in blood vessel endothelial cells, but not in the incisures of myelinated axons in peripheral nerves. Therefore, with the expectation that, similar to claudin-11

in oligodendrocytes, some specific claudin species are primarily expressed in Schwann cells, we examined the expression levels of newly identified claudin species (claudin-17 to -24) by using Northern blotting, and found that claudin-19 was expressed in large amounts in the PNS. Expectedly, immunofluorescence microscopy with anti–claudin-19 pAb revealed that claudin-19 was highly and characteristically abundant in paranodal loops, in outer/inner mesaxons, and in incisures where TJ-like structures have been detected by electron microscopy (Arroyo and Scherer, 2000; Poliak et al., 2002; Spiegel and Peles, 2002). Considering that in $Cld19^{-/-}$ mice, TJ-like structures completely disappeared (at least from the outer/inner mesaxons), it is safe to say that, similar to oligodendrocytes, Schwann cells also bear real TJs, and a single species of claudin (claudin-19) primarily constitutes them.

From the viewpoint of compartmentalization in myelinated axons, the intercellular sealing by the axo-glial paranodal junction is also important. This junction resembles the septate junction of invertebrates not only in appearance (Rosenbluth, 1976; Pedraza et al., 2001) but also in molecular organization. For example, Caspr/Paranodin (a single membrane-spanning protein) and protein 4.1B (a membrane skeleton protein) reportedly form a molecular complex at the vertebrate paranodal junction (Einheber et al., 1997; Menegoz et al., 1997; Peles et al., 1997; Arroyo and Scherer, 2000; Salzer, 2003), and at the invertebrate septate junctions, neurexin IV and coracle, which are homologous to Caspr/Paranodin and protein 4.1B, respectively, form a similar complex (Fehon et al., 1994; Baumgartner et al., 1996; Bellen et al., 1998). On the other hand, recent genetic analyses of *Drosophila melanogaster* mutants with a malformation of the trachea tube identified two *D. melanogaster* claudins, megatrachea and sinuous, which are localized at septate junctions, as being directly involved in the barrier function of tracheal epithelial cells (Behr et al., 2003; Wu et al., 2004). These findings naturally lead to speculation that also at the paranodal junctions of vertebrate PNS, some claudin or claudinlike membrane protein occurs to seal the axo-glial intercellular space. However, claudin-19 does not seem to be the putative paranodal claudin. Immunofluorescence microscopy revealed that in the paranodal region, claudin-19 was distributed more outwardly from Caspr-positive paranodal junctions themselves, and the septalike structures of paranodal junctions were not affected at the electron microscopic level in $Cld19^{-/-}$ mice. The possible relationship between paranodal junctions and claudins (or claudinlike molecules) should be examined in detail in the future.

In general, it is now believed that TJs play a key role not only in paracellular sealing but also in the establishment of epithelial cell polarity (Balda and Matter, 1998; Tsukita et al., 2001; Anderson et al., 2004). Through detailed genetical analyses with *Caenorhabditis elegans* and *D. melanogaster*, several protein complexes were identified as being directly involved in the cellular polarity (Gibson and Perrimon, 2003; Nelson, 2003; Roh and Margolis, 2003; Schneeberger and Lynch, 2004). These complexes were highly conserved throughout evolution, and among them, in vertebrates, PAR-3/aPKC/PAR-6, Crumbs3/PALS1/PATJ, and Scrib/mDlg/mLgl were shown to participate in the establishment of epithelial polarity by interacting with TJs. However, quite unexpectedly, $Cld19^{-/-}$ Schwann cells appeared to normally wrap their plasma membranes concentrically around the axon to form layers of compact myelin and the complicated structures of the node of Ranvier, though they lacked TJs. Furthermore, once-established myelin sheaths remained unaffected without showing any signs of demyelination up to at least 2 yr after birth. Therefore, although Schwann cells exhibited a very unique cellular morphogenesis, it would be reasonable to conclude that claudin-19–based TJs are not required for this polarized morphogenesis.

Finally, the question has naturally arisen as to what the real physiological function of claudin-19–based TJs in Schwann cells is. $Cld19^{-/-}$ mice exhibited significant behavioral abnormalities that were caused by PNS deficits. Based on an accumulated knowledge of TJs in the epithelia, it would be reasonable to speculate that these behavioral abnormalities are attributable to the defects in the electrical sealing by TJs in Schwann cells. However, compact myelin and the paranodal axo-glial junctions are also directly involved in the electrical sealing in Schwann cells, and it remains unclear how these structures are synergistically coordinated in the Schwann cell–based compartmentalization. Indeed, electrophysiological analyses of isolated peripheral nerves favored the notion that the saltatory conduction of myelinated axons itself was affected in $Cld19^{-/-}$ mice, showing peculiar double-peak CAP waveforms (Fig. 5). As it was technically difficult to clarify the molecular mechanism behind the generation of such peculiar CAP waveforms in $Cld19^{-/-}$ mice in more detail (at least in our hands) mainly because of the short length of isolated mouse sciatic nerves, it is still premature to further discuss the relationship between the behavioral abnormalities and double-peak CAP waveforms in $Cld19^{-/-}$ mice. Therefore, it is safe to say that these TJs were functionally indispensable for PNS myelinated axons.

The behavioral abnormalities of $Cld19^{-/-}$ mice were relatively mild, so that these mice grew normally and were fertile. Therefore, it is tempting to speculate about the possible existence of a human hereditary peripheral neuropathy; i.e., Charcot-Marie-Tooth (CMT) neuropathy caused by mutations in the claudin-19 gene. CMT is now known to show extensive genetic heterogeneity, and disease-causing mutations have been identified in different genes with a wide range of biological functions (Bertorini et al., 2004; Shy, 2004). The human claudin-19 gene is located at 1p34-1, and, interestingly, a recent analysis of two unrelated families with dominant, intermediate CMT narrowed down the responsible locus at 1p34-p35 (Jordanova et al., 2003). The possible involvement of claudin-19 mutations in this type of CMT should be examined in the future.

In this study, we identified claudin-19 as a major constituent of the TJ strands of Schwann cells and generated $Cld19^{-/-}$ mice. Schwann cells are unique in terms of cell morphogenesis, cell–cell adhesion, cell motility, etc. Therefore, the $Cld19^{-/-}$ mice will provide a valuable resource for studying not only the molecular events governing saltatory conduction but also the molecular mechanism underlying these general cellular events.

Materials and methods

Antibodies

Rabbit anti–mouse claudin-11 pAb was raised and characterized previously (Morita et al., 1999b). Mouse anti–pig neurofilament 200 pAb and rat anti–human myelin basic protein mAb were purchased from Sigma-Aldrich and Serotec Ltd., respectively. Rat anti–mouse E-cadherin mAb (ECCD2) was provided by M. Takeichi (Center for Developmental Biology, Kobe, Japan).

Anti–claudin-19 pAbs were raised in rabbits using keyhole limpet hemocyanin–conjugated peptide (MCL19 peptide) corresponding to the COOH-terminal 19 amino acids of mouse claudin-19. Antisera were affinity purified using beads coupled with MCL19 peptide before use. The specificity of these pAbs was confirmed by immunoblotting for GST fusion proteins with the COOH-terminal cytoplasmic tails of mouse claudin-1 to -16 (Morita et al., 1999b; Kiuchi-Saishin et al., 2002) and claudin-19.

Isolation of mouse claudin-19 cDNA and transfection

Mouse claudin-19 cDNA was isolated by RT-PCR. The first strand of cDNA was synthesized with the total RNA of a mouse kidney. PCR was performed with a primer set comprising a 5′ noncoding region primer (MCL19F, 5′-GCCTCCAGCTCCTGGGCTACTTC-3′) and a 3′ coding region primer including a stop codon (MCL19R, 5′-TCAGACGTACTCTCTG-GCAGCAGTTGA-3′). The nucleotide sequence of mouse claudin-19 cDNA that was obtained by RT-PCR was confirmed by directly sequencing the amplified fragments (sequence data are available from GenBank/EMBL/DDBJ under accession no. AF486651).

Mouse claudin-19 cDNA containing the entire coding region was subcloned into a pCAG-neo expression vector (Furuse et al., 1998b) or pCI-neo expression vector (Promega). These expression vectors were transfected into mouse L fibroblasts with lipofectamine plus (GIBCO BRL). Cells were plated on 10-cm dishes in DME medium supplemented with 10% FCS for 48 h and selected by adding G418 at a final concentration of 500 mg/ml. At day 14 of culture, the G418-resistant colonies were removed, and L cells stably expressing mouse claudin-19 were screened by immunofluorescent staining with claudin-19 pAb.

Generation of *Cld19*$^{-/-}$ mice

Three overlapping clones encoding mouse claudin-19 were obtained by screening a 129/Sv genomic library. Using one of them, the targeting vector was constructed as shown in Fig. 3 A. The diphthelia toxin A expression cassette (MC1pDT-A) was placed outside the 5′ arm of homology for negative selection. As shown in Fig. 3 A, four exons covered the whole ORF of claudin-19. Thus, this targeting vector was designed to delete all of these exons by replacing them with the pgk-neo cassette. J1 ES cells were electroporated with the targeting vector and selected for ~9 d in the presence of G418. The G418-resistant colonies were removed and screened with Southern blotting with the 5′ external probe (Fig. 3 B). When digested with XbaI, correctly targeted ES clones were identified by an additional 6.5-kb band together with the 10-kb band of the wild-type allele with the 5′ probe. The targeted ES cells obtained were injected into C57BL/6 blastocysts, which were in turn transferred into Balb/c foster mothers to obtain chimeric mice. Male chimeras were mated with C57BL/6 females, and agouti offspring were genotyped to confirm the germline transmission of the targeted allele. The littermates were genotyped with Southern blotting. Heterozygous mice were then interbred to produce homozygous mice.

Immunostaining

Transverse frozen sections of the mouse spinal cord with the ventral root or of the sciatic nerve (~6 μm thick) were cut on a cryostat, mounted on glass slides, air dried, and fixed in 95% ethanol at 4°C for 30 min followed by 100% acetone at RT for 1 min. They were then rinsed in PBS for 15 min, blocked with 1% BSA/PBS for 15 min, and incubated with primary antibodies. After washing with PBS three times, samples were incubated for 30 min with secondary antibodies. Cy3-conjugated goat anti–rat IgG (Amersham Biosciences) and Cy2-conjugated goat anti–rabbit IgG (Jackson ImmunoResearch Laboratories) were used as secondary antibodies. Samples were washed three times with PBS and mounted in 90% glycerol–PBS containing 0.1% para-phenylenediamine and 1% n-propylgalate. For whole-mount staining of sciatic nerves, mice were killed, and the nerves were removed in 0.1 M phosphate buffer. The nerves were teased, fixed, and whole-mount stained as described previously (Ishibashi et al., 2004). Specimens were observed using a photomicroscope (model Axiophot; Carl Zeiss MicroImaging, Inc.).

Northern blotting

The total RNA was isolated from mouse brain and sciatic nerves according to a method developed previously (Chomczynski and Sacchi, 1987), and aliquots of total RNA (1 μg) were separated with 1.0% agarose-formaldehyde gel electrophoresis and were transferred onto nylon membranes (Roche Diagnostics). For other tissues, mouse multiple tissue membranes (SeeGene) was used. Hybridization with a digoxigenin-labeled RNA probe, which was prepared from a PCR fragment amplified with primers MCL19F and MCL19R, was performed according to the manufacturer's protocol (Roche Diagnostics). After extensive washing, the membranes were incubated with CSPD (TROPIX) and exposed to X-ray films.

SDS-PAGE and immunoblotting

Lysates of *Escherichia coli* expressing GST/claudin fusion proteins were subjected to one-dimensional SDS-PAGE (12.5%), and gels were stained with Coomassie brilliant blue R-250 (Nacalai Tesque). For immunoblotting, proteins were electrophoretically transferred from gels onto polyvinylidene difluoride membranes, which were then incubated with the first antibody. Bound antibodies were detected with horseradish peroxidase–conjugated, secondary antibodies (Amersham Biosciences). ECLplus reagents (Amersham Biosciences) were used as substrates for the detection of peroxidase.

Electron microscopy

For ultrathin section electron microscopy, the saphenous nerve, which runs just beneath the skin along the thigh, was used in order to preserve the ultrastructural integrity of myelinated axons well (Tsukita and Ishikawa, 1980). Under ether anesthesia, the saphenous nerve was carefully exposed in 10-wk-old mice and was fixed in situ for 20 min with 2.5% glutaraldehyde and 2% formaldehyde in 0.1 M sodium cacodylate buffer, pH 7.2. Then, the nerve was removed together with the underlying muscle, and fixation was continued overnight at 4°C. In some samples, tannic acid was added to the fixative at a concentration of 0.1% to clearly visualize the kissing points of TJs. After being washed thoroughly with 0.1 M sodium cacodylate buffer, the nerve was cut into 1-mm-long segments, which were then postfixed in 1% OsO$_4$ in the same buffer for 2 h on ice. The segments were washed with distilled water and stained en bloc with 0.5% uranyl acetate for 2 h. They were dehydrated in ethanol and embedded in Epon 812. Thin sections were cut, double stained with uranyl acetate and lead citrate, and then examined under an electron microscope (model 1200EX; JEOL) at an accelerating voltage of 100 kV.

For freeze-fracture electron microscopy, sciatic nerves from 10-wk-old mice were fixed in 2% glutaraldehyde in 0.1 M sodium cacodylate buffer, pH 7.2, for 3 h at RT, washed with 0.1 M sodium cacodylate buffer three times, immersed in 30% glycerol in 0.1 M sodium cacodylate buffer for 2 h, and then frozen in liquid nitrogen. Frozen samples were fractured at −100°C and platinum shadowed unidirectionally at an angle of 45° in Balzers Freeze Etching System (model BAF060; Bal-Tec). The samples were then immersed in household bleach, and replicas floating off the samples were washed with distilled water. Replicas were picked up on formvar-filmed grids and examined with an electron microscope (model 1200EX; JEOL) at an acceleration voltage of 100 kV.

Behavioral tests

All behavioral tests were performed with male mice that were ~10–13 wk old at the start of the testing. Mice were housed in a room with a 12-h light/dark cycle (lights on at 7:00 a.m.) with access to food and water ad libitum. Behavioral testing was performed between 9:00 a.m. and 6:00 p.m. After the tests, all of the apparatus were cleaned with super hypochlorous water to deodorize the smell of mice.

Motor coordination and balance were assessed with the beam test and rotarod test. The beam (walking) test was adapted from Carter et al. (1999) by measuring the ability of mice to traverse a narrow beam to reach a dark box. The beams, with a rough painted surface, consisted of two different strips of iron (each measuring 100 cm long; one was 2.8 cm [thick bar] and the other was 1.1 cm [thin bar] in diameter) placed horizontally 50 cm above the bench surface. One session of five trials was performed using the 2.8-cm beam. Mice were then tested using the 1.1-cm beam. Mice were allowed up to 60 s to traverse each beam. The number of sideslips was recorded for each trial by the Image OF program (see the last paragraph of this section). The rotarod test using an accelerating rotarod (UGO Basile) was performed by placing a mouse on a rotating drum (3-cm diam) and by measuring the time each animal was able to maintain its balance on the rod. The speed of the rotarod was accelerated from 4 to 40 rpm over a 5-min period.

Locomotor activity was evaluated in the open field test. Each subject was placed in the center of the open field apparatus (40 × 40 × 30 cm;

Accuscan Instruments). Total distance traveled (cm), vertical activity (rearing measured by counting the number of photobeam interruptions), time spent in the center, and the beam-break counts for stereotyped behavior were recorded. Data were collected for 30 min.

To obtain an index of sensorimotor gating (the percent prepulse inhibition), the prepulse inhibition test was performed as described previously (Miyakawa et al., 2001). For this test, a startle reflex measurement system (O'Hara & Co.) was used. A test session began by placing a mouse in a plexiglas cylinder, where it was left undisturbed for 10 min. The duration of white noise that was used as the startle stimulus was 40 ms for all trial types. The startle response was recorded for 140 ms (measuring the response every 1 ms) starting with the onset of the prepulse stimulus. The background noise level in each chamber was 70 dB. The peak startle amplitude recorded during the 140-ms sampling window was used as the dependent variable. A test session consisted of six trial types (i.e., two types for startle stimulus-only trials, and four types for prepulse inhibition trials). The intensity of the startle stimulus was 110 or 120 dB. The prepulse sound was presented 100 ms before the startle stimulus, and its intensity was 74 or 78 dB. Four combinations of prepulse and startle stimuli were used (74–110, 78–110, 74–120, and 78–120). Six blocks of the six trial types were presented in pseudorandom order such that each trial type was presented once within a block. The mean intertrial interval was 15 s (range, 10–20 s).

The application used for the beam test (Image OF) was based on the public domain National Institutes of Health's Image program (developed by Wayne Rasband at the National Institute of Mental Health and available at http://rsb.info.nih.gov/nih-image/) and was modified for each test by Tsuyoshi Miyakawa (O' Hara & Co.). Statistical analysis was conducted using StatView (SAS Institute). Data were analyzed using the two-tailed t test, two-way analysis of variance between groups (ANOVA), or two-way repeated measures ANOVA, unless noted otherwise. Values in tables and graphs were expressed as the mean ± SEM.

Electrophysiological analyses

Conduction properties of myelinated axons were examined in sciatic-tibial nerves acutely isolated from 10-wk-old mice. Mice were anesthetized with sodium pentobarbital (Nembutal; 0.05 mg/g body weight, i.p.), and the nerve was carefully removed in a maximal length in Ringer's solution (147 mM NaCl, 4 mM KCl, and 2.2 mM CaCl$_2$). The nerve was placed on the Ag-AgCl electrodes arranged in the moist recording chamber. The electrodes of the proximal end of the nerve were connected to a stimulus isolator (model a55301J; Nihon Kohden), and those of the distal end were connected to an AC-coupled amplifier (gain, 1 k; band-pass filter, 1.5 Hz-1 kHz; model AB610J; Nihon Kohden) to record the CAP. The conduction distance of the nerve (the distance from the negative stimulating to recording electrode) was 25 mm in all experiments. All recordings were performed at RT (26–28°C). Each electrical stimulus was applied for a 100-μs duration, and an interval of 1 s was maintained between each stimulus. CAPs were monitored in real time on an oscilloscope and stored on a PC computer using a digitizer (model DIGIDATA 1322A; Axon Instruments, Inc.) for off-line analysis. The stored data were analyzed using pClamp9 (Axon Instruments, Inc.).

References

Anderson, J.M., and C.M. Van Itallie. 1995. Tight junctions and the molecular basis for regulation of paracellular permeability. *Am. J. Physiol.* 269:G467–G475.

Anderson, J.M., C.M. Van Itallie, and A.S. Fanning. 2004. Setting up a selective barrier at the apical junction complex. *Curr. Opin. Cell Biol.* 16:140–145.

Arroyo, E.J., and S.S. Scherer. 2000. On the molecular architecture of myelinated fibers. *Histochem. Cell Biol.* 113:1–18.

Balda, M.S., and K. Matter. 1998. Tight junctions. *J. Cell Sci.* 111:541–547.

Baumgartner, S., J.T. Littleton, K. Broadie, M.A. Bhat, R. Harbecke, J.A. Lengyel, R. Chiquet-Ehrismann, A. Prokop, and H.J. Bellen. 1996. A *Drosophila* neurexin is required for septate junction and blood-nerve barrier formation and function. *Cell.* 87:1059–1068.

Behr, M., D. Riedel, and R. Schuh. 2003. The claudin-like megatrachea is essential in septate junctions for the epithelial barrier function in *Drosophila. Dev. Cell.* 5:611–620.

Bellen, H.J., Y. Lu, R. Beckstead, and M.A. Bhat. 1998. Neurexin IV, Caspr and paranodin—novel members of the neurexin family: encounters of axons and glia. *Trends Neurosci.* 21:444–449.

Bertorini, T., P. Narayanaswami, and H. Rashed. 2004. Charcot-Marie-Tooth disease (hereditary motor sensory neuropathies) and hereditary sensory and autonomic neuropathies. *Neurologist.* 10:327–337.

Carter, R.J., L.A. Lione, T. Humby, L. Mangiarini, A. Mahal, G.P. Bates, S.B. Dunnett, and A.J. Morton. 1999. Characterization of progressive motor deficits in mice transgenic for the human Huntington's disease mutation. *J. Neurosci.* 19:3248–3257.

Chomczynski, P., and N. Sacchi. 1987. Single-step method of RNA isolation by acid guanidinium thiocyanate-phenol-chloroform extraction. *Anal. Biochem.* 162:156–159.

Dermietzel, R. 1974. Junctions in the central nervous system of the cat. I. Membrane fusion in central myelin. *Cell Tissue Res.* 148:565–576.

Dermietzel, R., and H. Kroczek. 1980. Interlamellar tight junctions of central myelin. I. Developmental mechanisms during myelogenesis. *Cell Tissue Res.* 213:81–94.

Einheber, S., G. Zanazzi, W. Ching, S. Scherer, T.A. Milner, E. Peles, and J.L. Salzer. 1997. The axonal membrane protein Caspr, a homologue of neurexin IV, is a component of the septate-like paranodal junctions that assemble during myelination. *J. Cell Biol.* 139:1495–1506.

Fannon, A.M., D.L. Sherman, G. Llyina-Gragerova, P.J. Brophy, V.L. Friedrich Jr., and D.R. Colman. 1995. Novel E-cadherin-mediated adhesion in peripheral nerve: Schwann cell architecture is stabilized by autotypic adherens junctions. *J. Cell Biol.* 129:189–202.

Farquhar, M.G., and G.E. Palade. 1963. Junctional complexes in various epithelia. *J. Cell Biol.* 17:375–412.

Fehon, R.G., I.A. Dawson, and S. Artavanis-Tsakonas. 1994. A *Drosophila* homologue of membrane-skeleton protein 4.1 is associated with septate junctions and is encoded by the coracle gene. *Development.* 120:545–557.

Furuse, M., T. Hirase, M. Itoh, A. Nagafuchi, S. Yonemura, and Sh. Tsukita. 1993. Occludin: a novel integral membrane protein localizing at tight junctions. *J. Cell Biol.* 123:1777–1788.

Furuse, M., K. Fujita, T. Hiiragi, K. Fujimoto, and Sh. Tsukita. 1998a. Claudin-1 and -2: novel integral membrane proteins localizing at tight junctions with no sequence similarity to occludin. *J. Cell Biol.* 141:1539–1550.

Furuse, M., H. Sasaki, K. Fujimoto, and Sh. Tsukita. 1998b. A single gene product, claudin-1 or -2, reconstitutes tight junction strands and recruits occludin in fibroblasts. *J. Cell Biol.* 143:391–401.

Gibson, M.C., and N. Perrimon. 2003. Apicobasal polarization: epithelial form and function. *Curr. Opin. Cell Biol.* 15:747–752.

Gow, A., C.M. Southwood, J.S. Li, M. Pariali, G.P. Riordan, S.E. Brodie, J. Danias, J.M. Bronstein, B. Kachar, and R.A. Lazzarini. 1999. CNS myelin and Sertoli cell tight junction strands are absent in Osp/claudin-11 null mice. *Cell.* 99:649–659.

Ishibashi, T., L. Ding, K. Ikenaka, Y. Inoue, K. Miyado, E. Mekada, and H. Baba. 2004. Tetraspanin protein CD9 is a novel paranodal component regulating paranodal junctional formation. *J. Neurosci.* 24:96–102.

Jordanova, A., F.P. Thomas, V. Guergueltcheva, I. Tournev, F.A. Gondim, B. Ishpekova, E. De Vriendt, A. Jacobs, I. Litvinenko, N. Ivanova, et al. 2003. Dominant intermediate Charcot-Marie-Tooth type C maps to chromosome 1p34-p35. *Am. J. Hum. Genet.* 73:1423–1430.

Kiuchi-Saishin, Y., S. Gotoh, M. Furuse, A. Takasuga, Y. Tano, and Sh. Tsukita. 2002. Differential expression patterns of claudins, tight junction membrane proteins, in mouse nephron segments. *J. Am. Soc. Nephrol.* 13:875–886.

Martin-Padura, I., S. Lostaglio, M. Schneemann, L. Williams, M. Romano, P. Fruscella, C. Panzeri, A. Stoppacciaro, L. Ruco, A. Villa, et al. 1998. Junctional adhesion molecule, a novel member of the immunoglobulin superfamily that distributes at intercellular junctions and modulates monocyte transmigration. *J. Cell Biol.* 142:117–127.

Menegoz, M., P. Gaspar, M. Le Bert, T. Galvez, F. Burgaya, C. Palfrey, P. Ezan, F. Arnos, and J.A. Girault. 1997. Paranodin, a glycoprotein of neuronal paranodal membranes. *Neuron.* 19:319–331.

Miyakawa, T., M. Yamada, A. Duttaroy, and J. Wess. 2001. Hyperactivity and intact hippocampus-dependent learning in mice lacking the M1 muscarinic acetylcholine receptor. *J. Neurosci.* 21:5239–5250.

Morita, K., M. Furuse, K. Fujimoto, and Sh. Tsukita. 1999a. Claudin multigene family encoding four-transmembrane domain protein components of tight junction strands. *Proc. Natl. Acad. Sci. USA.* 96:511–516.

Morita, K., H. Sasaki, K. Fujimoto, M. Furuse, and Sh. Tsukita. 1999b. Claudin-11/OSP-based tight junctions of myelin sheaths in brain and Sertoli cells in testis. *J. Cell Biol.* 145:579–588.

Morita, K., H. Sasaki, M. Furuse, and Sh. Tsukita. 1999c. Endothelial claudin: claudin-5/TMVCF constitutes tight junction strands in endothelial cells. *J. Cell Biol.* 147:185–194.

Mugnaini, E., and B. Schnapp. 1974. Possible role of zonula occludens of the myelin sheath in demyelinating conditions. *Nature.* 251:725–727.

Nelson, W.J. 2003. Adaptation of core mechanisms to generate cell polarity. *Nature.* 422:766–774.

Pedraza, L., J.K. Huang, and D.R. Colman. 2001. Organizing principles of the axo-glial apparatus. *Neuron.* 30:335–344.

Peles, E., and J.L. Salzer. 2000. Molecular domains of myelinated axons. *Curr. Opin. Neurobiol.* 10:558–565.

Peles, E., M. Nativ, M. Lustig, M. Grumet, J. Schilling, R. Martinez, G.D. Plowman, and J. Schlessinger. 1997. Identification of a novel contactin-associated transmembrane receptor with multiple domains implicated in protein-protein interactions. *EMBO J.* 16:978–988.

Peters, A. 1961. A radial component of central myelin sheaths. *J. Biophys. Biochem. Cytol.* 11:733–735.

Peters, A. 1964. Further observations on the structure of myelin sheaths in the central nervous system. *J. Cell Biol.* 20:281–296.

Poliak, S., S. Matlis, C. Ullmer, S.S. Scherer, and E. Peles. 2002. Distinct claudins and associated PDZ proteins form different autotypic tight junctions in myelinating Schwann cells. *J. Cell Biol.* 159:361–372.

Poliak, S., and E. Peles. 2003. The local differentiation of myelinated axons at nodes of Ranvier. *Nat. Rev. Neurosci.* 4:968–980.

Reale, E., L. Luciano, and M. Spitznas. 1975. Zonulae occludentes of the myelin lamellae in the nerve fibre layer of the retina and in the optic nerve of the rabbit: a demonstration by the freeze-fracture method. *J. Neurocytol.* 4:131–140.

Roh, M.H., and B. Margolis. 2003. Composition and function of PDZ protein complexes during cell polarization. *Am. J. Physiol. Renal Physiol.* 285:F377–F387.

Rosenbluth, J. 1976. Intramembranous particle distribution at the node of Ranvier and adjacent axolemma in myelinated axons of the frog brain. *J. Neurocytol.* 5:731–745.

Salzer, J.L. 2003. Polarized domains of myelinated axons. *Neuron.* 40:297–318.

Sandri, C., J.M. Van Buren, and K. Akert. 1977. Membrane morphology of the vertebrate nervous system. A study with freeze-etch technique. *Prog. Brain Res.* 46:1–384.

Schnapp, B., and E. Mugnaini. 1976. Freeze-fracture properties of central myelin in the bullfrog. *Neuroscience.* 1:459–467.

Schneeberger, E.E., and R.D. Lynch. 2004. The tight junction: a multifunctional complex. *Am. J. Physiol. Cell Physiol.* 286:C1213–C1228.

Shinowara, N.L., W.B. Beutel, and J.P. Revel. 1980. Comparative analysis of junctions in the myelin sheath of central and peripheral axons of fish, amphibians and mammals: a freeze-fracture study using complementary replicas. *J. Neurocytol.* 9:15–38.

Shy, M.E. 2004. Charcot-Marie-Tooth disease: an update. *Curr. Opin. Neurol.* 17:579–585.

Simon, D.B., Y. Lu, K.A. Choate, H. Velazquez, E. Al-Sabban, M. Praga, G. Casari, A. Bettinelli, G. Colussi, J. Rodriguez-Soriano, et al. 1999. Paracellin-1, a renal tight junction protein required for paracellular Mg^{2+} resorption. *Science.* 285:103–106.

Spiegel, I., and E. Peles. 2002. Cellular junctions of myelinated nerves. *Mol. Membr. Biol.* 19:95–101.

Staehelin, L.A. 1974. Structure and function of intercellular junctions. *Int. Rev. Cytol.* 39:191–283.

Tabira, T., M. J. Cullen, P. J. Reier, and H. deF. Webster. 1978. An experimental analysis of interlamellar tight junctions in amphibian and mammalian C.N.S. myelin. *J. Neurocytol.* 7:489-503.

Tetzlaff, W. 1978. The development of a zonula occludens in peripheral myelin of the chick embryo. A freeze-fracture study. *Cell Tissue Res.* 189:187–201.

Tetzlaff, W. 1982. Tight junction contact events and temporary gap junctions in the sciatic nerve fibers of the chicken during Wallerian degeneration and subsequent regeneration. *J. Neurocytol.* 11:839–858.

Tsukita, Sh., and H. Ishikawa. 1980. The movement of membranous organelles in axons. Electron microscopic identification of anterogradely and retrogradely transported organelles. *J. Cell Biol.* 84:513–530.

Tsukita, Sh., and M. Furuse. 1999. Occludin and claudins in tight-junction strands: leading or supporting players? *Trends Cell Biol.* 9:268-273.

Tsukita, Sh., M. Furuse, and M. Itoh. 2001. Multifunctional strands in tight junctions. *Nat. Rev. Mol. Cell Biol.* 2:285–293.

Turksen, K., and T.C. Troy. 2004. Barriers built on claudins. *J. Cell Sci.* 117:2435–2447.

Van Itallie, C.M., and J.M. Anderson. 2004. The molecular physiology of tight junction pores. *Physiology.* 19:331–338.

Wu, V.M., J. Schulte, A. Hirschi, U. Tepass, and G.J. Beitel. 2004. Sinuous is a *Drosophila* claudin required for septate junction organization and epithelial tube size control. *J. Cell Biol.* 164:313–323.